Accepted Manuscript

Hydrogen transport in metals: Integration of permeation, thermal desorption and degassing

E.I. Galindo-Nava[1], B.I.Y. Basha[1], P.E.J. Rivera-Díaz-del-Castillo[2*]

[1] Department of Materials Science and Metallurgy, University of Cambridge

27 Charles Babbage Rd, Cambridge CB3 0FS, UK

[2] Department of Engineering, Lancaster University

Lancaster LA1 4YW, UK

*email: p.rivera1@lancaster.ac.uk, +44 1524 592439

Abstract

A modelling suite for hydrogen transport during electrochemical permeation, degassing and thermal desorption spectroscopy is presented. The approach is based on Fick's diffusion laws, where the initial concentration and diffusion coefficients depend on microstructure and charging conditions. The evolution equations are shown to reduce to classical models for hydrogen diffusion and thermal desorption spectroscopy. The number density of trapping sites is found to be proportional to the mean spacing of each microstructural feature, including dislocations, grain boundaries and various precipitates. The model is validated with several steel grades and polycrystalline nickel for a wide range of processing conditions and microstructures. A systematic study of the factors affecting hydrogen mobility in martensitic steels showed that dislocations control the effective diffusion coefficient of hydrogen. However, they also release hydrogen into the lattice more rapidly than other kind of traps. It is suggested that these effects contribute to the increased susceptibility to hydrogen embrittlement in martensitic and other high–strength steels. These results show that the methodology can be employed as a tool for alloy and process design, and that dislocation kinematics play a crucial role in such design.

Keywords: Hydrogen; Diffusion; Modelling; Trapping; Permeation; Desorption

1 Introduction

Prescribing hydrogen transport is critical to understand hydrogen embrittlement in metals, including ingress, storage and release [1]. These mechanisms depend on the ability for hydrogen to enter and diffuse within the bulk as various lattice imperfections act as trapping sites [2]. The surface represents an initial energy well for hydrogen to ingress and initialise diffusion in the metal [3], whilst the hydrogen located in the traps must overcome a binding energy larger than that for lattice diffusion before it can be released [1]. A number of experimental methods have been employed to study hydrogen diffusion in metals with distinct microstructures. For instance, electrochemical permeation testing (EP) has been used to determine the rate of adsorption of electrolytic hydrogen and its subsequent diffusivity [4, 5]. Similarly, thermal desorption spectroscopy (TDS) has been widely employed to estimate the trap binding energy by indirectly measuring the rate of hydrogen release during continuous heating [1]. Although these techniques provide good insights into hydrogen transport for a given material, they are highly sensitive to charging/heating conditions, the geometry of the specimen and initial microstructure [6–9]. Hence, modelling methods are needed to quantitatively interpret hydrogen–microstructure interactions in complex systems, such as the case of high–strength steels.

Oriani [2] has proposed a thermodynamic model based on local equilibrium between the hydrogen situated in the lattice and in the traps. This assumption allows obtaining a direct relationship between the equilibrium hydrogen concentration in the lattice (c_L) and in the traps (c_t), as well as estimating the effective diffusion coefficient including trapping effects:

$$
\begin{aligned}
c_t &= c_L \frac{N_t}{N_l} \exp\left(\frac{E_b}{R_{gas}T}\right) \\
D &= \frac{D_0 \exp\left(-\frac{Q}{R_{gas}T}\right)}{1 + \frac{N_t}{N_l} \exp\left(\frac{E_b}{R_{gas}T}\right)},
\end{aligned}
\tag{1}
$$

where N_l and N_t are the total lattice and trapping sites in the material, respectively, E_b is the trap binding energy with hydrogen, Q is the activation energy for hydrogen lattice

diffusion, D_0 is the lattice diffusion coefficient prefactor, R_{gas} is the gas constant and T is the absolute temperature. These equations do not account for kinetic effects and hydrogen interactions with the traps. Similarly, Fischer *et al.* [10] have also used the local equilibrium assumption to describe interstitial diffusion in metals with multiple trapping species.

A number of models for mass transport and desorption have been proposed to understand hydrogen diffusion under the presence of single or multiple trap species [3, 11–16]. For instance, Choo and Lee [1] applied the Kissinger equation [11] to describe the rate of hydrogen release during thermal desorption spectroscopy; although this relationship has been widely applied to estimate E_b via identifying the peak temperature T_c (maximum desorption rate) [17–19], it has been shown that the sample dimensions and density of traps affect T_c [9,16]. Another important approach for hydrogen transport was introduced by McNabb and Foster [12]. They proposed two coupled diffusion equations for lattice (c_L) and trapped (c_t) hydrogen, where the rates of capture and escape depend on E_b. This model has been applied to study permeation and desorption tests [20, 21], however it requires a number of parameters to be identified.

Due to the need to incorporate various fitting parameters, these models fall short in identifying optimal microstructures for hydrogen resistance, especially when various metallic systems are considered. Another implication of these limitations is the scatter in trapping parameter values reported by different authors [22–24]. This issue is critical in materials susceptible to hydrogen embrittlement due to the presence of multiple trap species altering the overall mobility of hydrogen. Moreover, it has been observed experimentally that the apparent diffusivity during electrochemical permeation not only depends on the microstructure but also on the charging conditions [8, 22]. This shows that, in spite of the previous results, there is no unified description for hydrogen transport able to describe hydrogen permeation, desorption and release, including the relevant processing parameters, sample geometries and microstructural features. The wide application of Oriani's equations to estimate hydrogen diffusivity in various materials suggests that, to some extent, local–equilibrium may hold for the time and length scales of EP

and TDS, and for low H content. This also implies that Fickian diffusion models could be sufficient to describe hydrogen diffusion.

The objective of this work is to introduce a unified description for hydrogen transport combining electrochemical permeation, thermal desorption and degassing. This is to define a methodology for process design and to identify optimal microstructures reducing hydrogen diffusivity. The formulation is based on postulating Fickian diffusion equations including the relevant microstructural features, testing conditions and (three–dimensional) geometries affecting the overall diffusion behaviour. An expression for the apparent diffusion coefficient during permeation D_{perm} including the effects of charging conditions and microstructural features is obtained. Additionally, using the local equilibrium assumption to compute the diffusion coefficient, it is possible to estimate the egress of hydrogen when various microstructural features act as trapping sites. This allows to consolidate the descriptions for diffusion during ingress, storage and release adopting the same set of parameters for various alloy grades and similar microstructures. This is demonstrated by applying the models to several steel grades, including ferritic, martensitic, bainitic, pearlitic and austenitic, as well as in polycrystalline nickel. A parametric analysis on hydrogen transport in martensitic steels, a system with multiple kinds of traps, is performed to understand the role of different microstructural features in trapping events.

2 Modelling transport kinetics during electrochemical charging

Electrochemical charging allows to measure the hydrogen permeation rate and the apparent diffusion within a metal. There are two regimes during permeation [4, 25, 26]: I) a transient region induced by electrochemical reactions at the sample's surface; and II) a steady state, where the variation in the concentration and current density is constant. Additionally, electrochemical charging is widely employed for thermal desorption spectroscopy studies to increase the hydrogen content in the material to understand trapping

behaviour. Hence, it is also important to study hydrogen ingress not only to understand diffusion but also to provide the initial spatial concentration distribution of hydrogen for TDS.

The H permeation rate depends on several factors including oxide layer formation, cathodic current density, sample dimensions and internal microstructure [4,5,26,27]. Permeation can be described by standard diffusion equations if it is assumed that the oxide layer represents an additional energy barrier for diffusion [4,28]. This assumption is valid when the sample thickness is larger than ~ 0.1 mm [28,29]. The cathodic current density (I_c) affects permeation by modifying the rate at which hydrogen atoms are introduced into the metal by electrochemical reactions. However, increasing I_c not only affects the steady–state permeation rate (effective H concentration) but it also accelerates the transport of H through the sample [8,30]. Hence, the net mass flux within the specimen (J) should include the contributions of diffusion in the lattice and traps J_{diff} and diffusion promoted by electrochemical charging J_{chem}:

$$J = J_{diff} + J_{chem}. \tag{2}$$

The H concentration profile in the sample is determined by the density of traps and Figure 1(a) shows a schematic representation of the diffusion landscape for hydrogen in one dimension: after it enters the sample from the cathodic polarisation and overcomes E_{perm} (left), the permeation (oxidation) activation energy, hydrogen atoms will diffuse in the lattice until they encounter a trap (concentration well)*. The trap landscape depends on the microstructure and it is described by the function $c_{well}(x)$, where the saturation concentration is $c(x) = c_{sat}$ for x within the trapping wells (Fig. 1(a)), and $c_{well}(x) = 0$ for x different to the interval x_0, where a trap is located. Hydrogen atoms are adsorbed to a trap (gray areas) until the well is saturated and the remaining hydrogen atoms continue diffusing across the lattice until finding the next trap. Figure 1(b) shows a one–dimensional representation of the energy landscape for hydrogen diffusion†. Although an

---

*Only one kind of trap is considered in the description of permeation, degassing and thermal desorption; the extension to multiple trap species is presented in Section 5.

†It is worth noting that in a three dimensional scenario hydrogen diffusion will not be necessarily

additional energy barrier might be required for hydrogen to enter the traps [31], it will be assumed null since there is limited experimental information on how this barrier affects the diffusion profile.
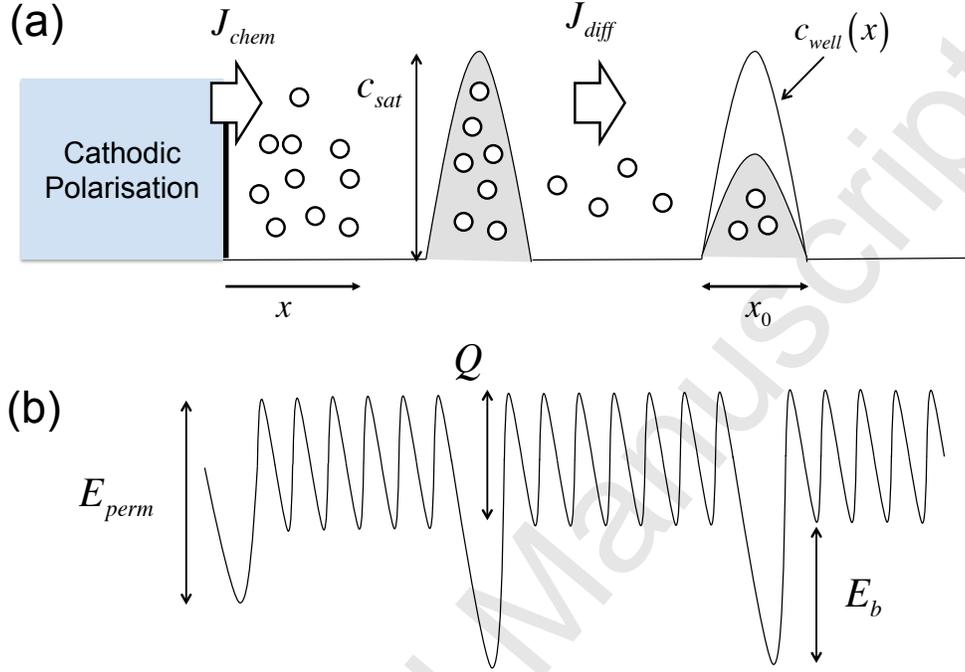

Figure 1: Schematic representation of the (a) energy and (b) concentration landscape for hydrogen transport in the traps.

This results in J_{diff} being by given the difference between $c_{well}(x)$ and the actual concentration in the sample [32]:

$$J_{diff} = -D\nabla\big(c_{well} - c_{perm}\big), \tag{3}$$

where D is the diffusion coefficient in the material (equation 1). Although the diffusivity of hydrogen varies locally due to the inhomegeneous energy landscape (Figure 1(b)), in order to define an apparent diffusion coefficient, we consider a homogeneous trapping landscape to avoid describing local variations in the diffusion parameters. This is consistent with the assumption of local equilibrium between the free and trapped hydrogen atoms employed to estimate D in equation 1 [2]. Frappart et al. [22] have suggested that the apparent diffusion

restricted to pass through the trap, as opposed to a one–dimensional domain.

coefficient during permeation can be determined considering the system (steel + oxide layer) as a homogeneous representative volume element. This is done by incorporating an additional term in the activation energy for hydrogen lattice diffusion, $Q + E_{perm}$, in equation 1, where E_{perm} accounts for the increase in the energy barrier due to hydrogen ingress [22]. E_{perm} has been found to hold values for iron and nickel in the range [4, 5, 27, 33, 34]: 11 ± 2 kJ/mol. $E_{perm} = 13$ kJ/mol will be assumed for both systems, including iron in the austenitic phase.

Faraday's law dictates that the rate of hydrogen atoms liberated to the metal's sub-surface (J_{chem}) is controlled by the rate of electric charge passing through the sample at a given time. This has been found to be proportional to $I_c^{1/2}$, the lattice diffusion coefficient D_0, and the variation in the concentration of the absorbed hydrogen into the specimen, $\nabla(c_{well} - c_{perm})$ [4, 5, 35]:

$$J_{chem} = -\kappa\sqrt{I_c}\left(1 + \frac{N_t}{N_l}\exp\left(\frac{E_b}{R_gT}\right)\right)D_0\nabla(c_{well} - c_{perm}), \qquad (4)$$

where κ is a constant and $\left(1 + \frac{N_t}{N_l}\right)$ accounts for the interactions between absorbed hydrogen atoms into the sample and the effective fraction of sites for diffusion (lattice and traps): the 1 factor represents the fraction of available lattice sites and $\frac{N_t}{N_l}\exp\left(\frac{E_b}{R_gT}\right)$ is the fraction of H atoms interacting with trapping sites. The evolution equation for the hydrogen concentration is obtained by applying Fick's second law:

$$\begin{aligned}
\frac{\partial c_{perm}}{\partial t} &= \nabla(J_{diff} + J_{chem}) = D_{perm}\nabla^2(c_{well} - c_{perm}), \\
D_{perm} &= D + \kappa\sqrt{I_c}\left(1 + \frac{N_t}{N_l}\exp\left(\frac{E_b}{R_gT}\right)\right)D_0
\end{aligned} \qquad (5)$$

with D_{perm} being the apparent diffusion coefficient. $\kappa = 9 \times 10^{-5}$ m A$^{-1/2}$ was adjusted for ferritic, martensitic, bainitic and pearlitic steels, whereas $\kappa = 2 \times 10^4$ m A$^{-1/2}$ was adjusted for austenitic steels. Similarly, $\kappa = 50$ m A$^{-1/2}$ was fitted for pure nickel. It is interesting noting that D_{perm} not only includes effects from the microstructure (via D, N_t and E_b), but it also accounts for variations in the charging current density. Moreover, if electrochemical permeation is absent ($I_c = 0$), $D_{perm} = D$ and an equation for homogeneous lattice

7

diffusion is recovered. This will be explored in the next section.

Equation 5 can be solved for a cylindrical sample of radius R and length L (Figure 2(a)), by applying the method of separation of variables: $c_{perm} = \Theta_{mn}(t)R_n(r)Z_m(z)$. It is worth noting that the variation of c_{well} with r and z is the same as c_{perm}, since the traps determine the diffusion profile within the sample [28], $i.e.$ $c_{well} = c_{sat}R_n(r)Z_m(z)$. Equation 5 is then expressed:

$$R_n Z_m \Theta'_{mn} = D_{perm}(c_{sat} - \Theta_{mn})\left(R''_n Z_m + \frac{1}{r}R'_n Z_m + R_n Z''_m\right), \tag{6}$$

which represents a set of three ordinary differential equations that individually depend on t, r and z and can be solved by conventional methods.
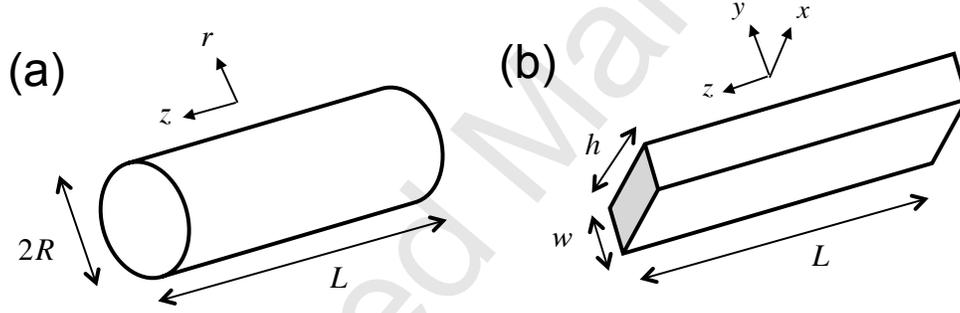

Figure 2: Schematic representation of a (a) cylindrical and (b) plate geometry.

If there is no hydrogen initially in the sample, the initial condition is set $c_{perm}(r, z, 0) = 0$. Additionally, since the density of traps determines the steady state permeation flux [36], the boundary conditions are set to correspond to a constant concentration c_{sat} at the surface of the sample ($r = R$ and $z = -L/2, L/2$); this is mathematically expressed as: $c_{perm}(R, z, t) = c_{sat}$, $\frac{\partial c_{perm}}{\partial r}(R, z, t) = 0$ and $c_{perm}(r, -L/2, t) = c_{perm}(r, L/2, t) = c_{sat}$, $\frac{\partial c_{perm}}{\partial z}(r, -L/2, t) = \frac{\partial c_{perm}}{\partial z}(r, L/2, t) = 0$. The solution of equation 5 with these conditions is given by the series [37]:

$$c_{perm}(r, z, t) = c_{sat} \sum_{m,n=0}^{\infty} \left(1 - \exp(-D_{perm}(\lambda_n^2 + \alpha_m^2)t)\right) R_n Z_m, \tag{7}$$

where $\lambda_n = \frac{4n-1}{4R}\pi$ and $\alpha_m = \frac{\pi}{L}m$ are the eigenvalues of equation 5, and $R_n = \frac{2}{R\lambda_n J_1(\lambda_n R)}J_0(\lambda_n r)$

and $Z_m = \frac{4}{L\alpha_m} \sin(\frac{\pi}{2}m) \cos(\alpha_m z)$ are the eigensolutions along r and z, respectively; J_0 is the Bessel function of first kind and zero order in r. An analogous solution for a plate–shaped specimen is shown in Appendix. Equation 7 allows us to determine the hydrogen concentration profile if the apparent diffusion coefficient is known.

2.1 Initial concentration

Several authors have found that the saturation concentration of hydrogen c_{sat} increases with the steady state permeation density I_∞, via the increase in the charging density (I_c) according to [9, 21, 30, 33, 38]‡: $c_{sat} \propto I_\infty \propto I_c^{1/2} \exp\left(-\frac{E_{perm}+Q}{R_{gas}T}\right)$. Additionally, the saturation concentration in the trapping wells depend on the total number density of trapping sites N_t [7]. These results are combined to obtain c_{sat}:

$$c_{sat} = n_0 \sqrt{I_c} \exp\left(-\frac{E_{perm}+Q}{R_{gas}T}\right) \frac{N_t}{N_l} A_{surf}, \tag{8}$$

where n_0 [H atoms m / A$^{1/2}$] is a constant that depends on the electrochemical solution, and A_{surf} is the surface area of the sample that is exposed to electrochemical charging [39]. The concentration profile in the specimen during permeation is obtained by combining equations 7 and 8.

It is worth noting that equation 8 does not include the exponential term shown in equation 1, where $c_t \propto N_t \exp\left(\frac{E_b}{R_{gas}T}\right)$. This factor is considered to affect hydrogen diffusion (via D_{perm}), whereas c_{sat} is controlled by the number of trapping sites available in the material (N_t). This result is consistent with experimental measurements of hydrogen concentration in different kinds of traps. For instance, Wei and Tsuzaki [40] have found that the binding energy of incoherent and semicoherent Ti carbides is 85 kJ/mol and 55.8 kJ/mol, respectively; this indicates that at room temperature the factor $\exp\left(\frac{E_b}{R_{gas}T}\right)$ of incoherent and semicoherent carbides is 8×10^{14} and 6×10^9. This suggests that, based on equation 1 and if N_t in both carbides has a similar order of magnitude, the concentration of hydrogen trapped at incoherent carbides can be up to 5 orders of magnitude higher

---

‡An equivalent expression can be obtained for hydrogen gas applied under a pressure P, where I_c is replaced by P.

9

than at coherent carbides. However, this result contradicts the estimated concentrations from TDS, where higher hydrogen content was measured in semicoherent carbides [39,41]. Similarly, Depover *et al.* [19] have compared the trapping capacity in martensitic steels containing semicoherent Ti and Mo carbides. The binding energy for molybdenum carbides has been estimated to be $E_b \approx 30$ kJ/mol [42], resulting in $\exp\left(\frac{E_b}{R_{gas}T}\right) = 1.8 \times 10^5$; this indicates that, based on equation 1, c_t in the Ti carbides would be up to 4 orders of magnitude higher than in the Mo precipitates of similar size and phase fraction. However, they found that the concentration profiles in as–quenched and aged conditions did not vary substantially. Additionally, equation 8 is consistent with experimental findings showing that hydrogen remains at the interface of the TiC [41], hence its concentration being only dictated by the density of trapping sites. However, these effects might also be controlled by the effective energy barrier for hydrogen to ingress in the trap and further theoretical investigation would be required to quantify these effects [31,43]. These results indicate that E_b should mainly affect the H diffusion profile and N_t controls the saturation concentration.

3   Transport kinetics during degassing

Vacuum degassing is a standard process during manufacturing of a high-strength component to reduce the hydrogen content in the material and decrease its susceptibility to hydrogen embrittlement. It has been suggested that hydrogen captured by traps with low binding energy escapes out of specimen during this process, traps with high E_b are able to store hydrogen for a longer time [44, 45]. From a process design point of view it is interesting to assess the efficiency of the traps when a number of microstructures are present. Additionally, degassing is commonly employed as an intermediate step between electrochemical charging and thermal desorption spectroscopy.

Degassing can be modelled following the same methodology than in the previous section. In this case, the net mass flux within the specimen (J_{degas}) is given only by the flux of the trapping wells releasing the hydrogen from the sample into the environment, as

10

$I_c = 0$ [22]; this is mathematically expressed as:

$$J_{degas} = -D\nabla c_{degas} \tag{9}$$

where c_{degas} is the concentration of hydrogen in the traps during degassing, and D is the material's H diffusion coefficient. Since there is no external flux during degassing, it can be assumed that D is solely controlled by the rate of hydrogen being released at the traps and employ equation 1. Using Fick's second law a standard diffusion equation for a cylindrical specimen is obtained for c_{degas} which solution,

$$c_{degas}(r, z, t) = c_{0,degas} \sum_{m,n=0}^{\infty} \exp(-D(\lambda_n^2 + \alpha_m^2)t) R_n Z_m, \tag{10}$$

satisfies the initial condition (concentration) $c_{degas}(r, z, 0) = c_{0,degas}$ and boundary conditions such that a constant concentration $c_{0,degas}$ at the surface of the sample is held throughout degassing, $i.e.$: $c_{degas}(R, z, t) = c_{0,degas}$, $\frac{\partial c_{degas}}{\partial r}(R, z, t) = 0$ and $c_{degas}(r, -L/2, t) = c_{degas}(r, L/2, t) = c_{0,degas}$, $\frac{\partial c_{degas}}{\partial z}(r, -L/2, t) = \frac{\partial c_{degas}}{\partial z}(r, L/2, t) = 0$. The formulation for c_{degas} in a plate–shaped sample is shown in the Appendix. This result is consistent with similar models for degassing [44, 45], however in this case we will consider the role of microstructure explicitly. The combination of equations 1 and 10 allow us to obtain the concentration profile during degassing hydrogen in the specimen. This solution will also enable us to describe hydrogen release during thermal desorption when degassing is an intermediate step between electrochemical charging and TDS.

4   Transport kinetics during thermal desorption

Thermal desorption spectroscopy accelerates hydrogen release by continuous heating and rapidly decreasing the concentration of hydrogen (c_{desorp}) in the sample. Hydrogen release from the specimen is monitored as a function of temperature (or time), where the peaks in the desorption rate ($\frac{dc_{desorp}}{dt}$) correspond to the hydrogen located in the traps. The solution of the equation for hydrogen desorption holds the same form as equation 10 with

initial concentration $c_{0,desorp}$:

$$c_{desorp}(r, z, t) = c_{0,desorp} \sum_{m,n=0}^{\infty} \exp(-D(\lambda_n^2 + \alpha_m^2)t)R_n Z_m. \tag{11}$$

This equation is differentiated with respect to t to obtain the desorption rate. For a constant heating rate ϕ, the desorption rate equals [§]:

$$\frac{dc_{desorp}}{dt} = c_{0,desorp}\left(D + \frac{dD}{dt}t\right) \sum_{m,n=0}^{\infty} (\lambda_n^2 + \alpha_m^2) \exp(-D(\lambda_n^2 + \alpha_m^2)t)R_n Z_m \tag{12}$$

The diffusion coefficient varies according to (equation 1):

$$\frac{dD}{dt} = \frac{D_0 \exp\left(-\frac{Q}{R_{gas}T}\right)}{\left(1 + \frac{N_t}{N_l}\exp\left(\frac{E_b}{R_{gas}T}\right)\right)} \left(\frac{Q}{R_{gas}T^2} + \frac{\frac{N_t}{N_l}\exp\left(\frac{E_b}{R_{gas}T}\right)}{\left(1 + \frac{N_t}{N_l}\exp\left(\frac{E_b}{R_{gas}T}\right)\right)}\frac{E_b}{R_{gas}T^2}\right)\phi. \tag{13}$$

Thermal desorption profiles can be obtained combining equations 12 and 13. A similar description for plate–shaped sample geometry is shown in the Appendix. The results allow us to have a unified description of hydrogen transport under different scenarios if the trapping parameters are known.

5 Trapping parameters and multiple trap species

One of the most important aspects of the model is determining the trapping parameters for a given material. The binding energies of the microstructural features included in this study have been estimated experimentally and using atomistic simulations by several authors; however, in most cases the scatter in the energies is wide. Table 1 shows the range of values of E_b and the values employed in this work for the microstructures under consideration. These values are fixed constant for all alloys tested. The binding energy of lamellar cementite (pearlite) is considered higher, as this structure strongly alters hydrogen migration paths [46]. This increases the probability for hydrogen to become trapped at the interior of the lamellae, which binding energy is higher than at the ferrite/cementite

---

[§]A negative sign is added to this equation to describe the rate of loss in concentration during desorption.

12

interface [43].

Table 1: Binding energies of the traps tested in this work.

Trap	E_b (kJ/mol)	This work (kJ/mol)	Author
Dislocations	25–60	26.8	[1, 16, 47]
Grain boundaries	17–50	17.2	[1, 48]
Cementite	33–60	30	[43]
Pearlitic cementite	33–60	43	[43]
M_2C	25–30	30	[42, 49]
M_4C_3	6–116	35	[31, 42]

As for the density of trapping sites, we highlight the fact that the diffusion length of hydrogen is dictated by the mean free path of the traps. The encountering frequency of hydrogen in the lattice and the trapping wells should be proportional to the mean spacing of the respective microstructural feature Λ, $i.e.$, $\frac{N_t}{N_l} = \frac{r_t}{\Lambda}$, where r_t is the width of the trap. For the case of dislocations Λ is given by the mean dislocation spacing $(1/\sqrt{\rho}$, where ρ is the dislocation density) and $r_t = \pi b$ [16], where b is the Burgers vector; similarly, for grain boundaries Λ equals the mean grain size D_g and $r_t = b$ [16]. For the case of finely dispersed spherical precipitates, $\Lambda_p = r_p \left(\frac{\pi}{f_p}\right)^{1/2}$¶, where f_p is the volume fraction and r_p is the mean radius. Since hydrogen atoms can be trapped at any location of the particle's interface, an additional factor is included; it equals the surface area width per unit volume [50]: $\frac{A_p b}{V_p} = \frac{3b}{r_p}$. r_t is considered as half the arc-length of the particle πr_p. The number density of these traps equals:

$$\begin{aligned}
\frac{N_{dis}}{N_l} &= \frac{\pi b}{\Lambda_{dis}} = \pi b \sqrt{\rho} \\
\frac{N_{grain}}{N_l} &= \frac{b}{\Lambda_{dis}} = \frac{b}{D_g} \\
\frac{N_p}{N_l} &= \frac{\pi r_p}{\Lambda_p} \frac{A_p b}{V_p} = \frac{3\pi^{1/2} f_p^{1/2}}{r_p},
\end{aligned} \tag{14}$$

¶The mean spacing between particles is considered in two dimensions, since most of the experimental characterisation has been performed using two–dimensional images.

where Equations 14 provide a direct link between microstructure and trapping densities; N_{dis}, N_{grain} and N_p stand for the number density of traps at dislocations, grain boundaries and precipitates, respectively.

When multiple species of non–interacting traps are present in the sample, it has been shown experimentally using TDS that the total concentration of hydrogen can be estimated by adding the individual concentration of the thermal desorption peaks [17, 18, 41]. This is also consistent with modelling results showing that the increase in hydrogen content is the summation of the contribution of all the traps present in the sample [10]. Moreover, since Fickian diffusion equations are linear, the concentration of hydrogen under the presence of multiple traps in our models is simply dictated by the summation of the individual contributions of each kind of trap (i): a trapping well with different traps is the summation of the wells, $i.e.$ $c_{well}(x) = \sum_i c_i^{well}(x)$, where each kind of trap has a saturation concentration c_i^{sat}; c_{perm} is split into the permeation concentration stemming from each trapping well $c_{perm} = \sum_i c_i^{perm} = \sum_i \Theta_i^{mn} R_n Z_m$, where Θ_i^{mn} is the time–dependent permeation concentration due to trap i. The permeation flux is equal to the net flux in all traps:

$$J = -\sum_i D_i^{perm}(\nabla c_i^{well} - \nabla c_i^{perm}). \tag{15}$$

Equation 6 now becomes: $\sum_i R_n Z_m \Theta'_{mn,i} = \sum_i D_i^{perm}\left(c_i^{sat} - \Theta_{mn,i}\right)\left(R''_n Z_m + \frac{1}{r} R'_n Z_m + R_n Z''_m\right)$, which solution is simply the summation of the individual solutions. An analogous description can be made to show that this result holds during degassing and permeation. The concentration evolution during permeation, degassing and thermal desorption due to different kinds of traps is equal to:

$$
\begin{aligned}
c_{perm} &= \sum_i c_{perm,i} \\
c_{degas} &= \sum_i c_{degas,i} \\
\frac{dc_{desorp}}{dt} &= \sum_i \frac{dc_{desorp,i}}{dt},
\end{aligned}
$$

$$\tag{16}$$

14

where the respective trapping parameters and initial concentrations are identified individually using the results in Sections 2, 3 and 4. This result allows us to deconvolute in a simple and efficient fashion the contributions of distinct microstructures affecting hydrogen transport. These models results are now tested under different conditions and microstructures.

6 Materials and methods

The models for hydrogen transport are compared against experimental data obtained from the literature and data produced in this work. Hydrogen charging, degassing and desorption were experimentally studied on three steel grades: 100Cr6, 100Cr6+0.5V and 100CrMnMoSi8-4-6; the first two alloys are fully martensitic, whereas the latter is fully bainitic. Table 2 shows the chemical composition of the materials tested. This covers a variety of steel grades, including 4 ferritic, 5 martensitic, 3 pearlitic, 1 bainitic and 3 austenitic, as well as 3 tests in pure nickel. It is interesting to note that Mart/Pearl was tested as tempered martensite and cold–drawn pearlite to compare the influence on the microstructure in the same steel grade [17].

Another important aspect to consider is the geometry of the sample for each material tested. Table 3 shows the shape and dimensions of the samples tested in this work. These values were obtained from the original reference. Cylindrical and plate–like samples are mostly used in the experiments. No sample length was reported in Mart/Pearl and $L = 20$ mm was assumed. Similarly, for Nickel B and Nickel C $w = h = 20$ mm were assumed since these values were not reported. For the case of Ferritic C, $L = 1$ mm was considered.

Table 2: Chemical composition (in wt%) of the materials tested in this work.

Steel	Fe	C	Mn	Si	Cr	Ni	Al	Mo	V	Ref.
Ferritic A	Bal.	-	-	-	-	-	-	-	-	[8]
Ferritic B	Bal.	0.002	0.12	0.005	-	0.02	0.21	-	-	[51]
Ferritic C	Bal.	0.004	0.078	-	-	-	0.046	-	-	[16]
Ferritic D	Bal.	-	-	-	-	-	-	-	-	[1]
Martensitic A	Bal.	0.45	-	-	-	-	-	1.5	-	[22]
Martensitic B	Bal.	0.38	0.5	0.12	1.34	3.12	-	0.43	0.2	[45]
Mart/Pearl	Bal.	0.82	0.78	0.23	0.18	-	-	-	-	[17]
Pearlitic A	Bal.	0.84	0.73	0.25	-	-	-	-	-	[18]
Pearlitic B	Bal.	0.82	0.77	0.12	-	-	-	-	-	[44]
100Cr6	Bal.	0.974	0.276	0.28	1.38	0.184	0.042	0.056	-	This study
100Cr6+0.5V	Bal.	0.974	0.28	0.27	1.42	0.01	0.003	0.093	0.55	This study
100CrMnMoSi8-4-6	Bal.	1	0.9	0.45	2	0.15	0.5	0.5	-	This study
TWIP	Bal.	0.6	18	-	-	-	-	-	-	[52]
AISI 310	Bal.	0.05	0.88	0.56	25.54	19.09	-	0.24	-	[53]
AISI 301	Bal.	0.05	1.28	0.48	17.1	7.25	-	0.24	-	[54]
Nickel A	-	-	-	-	-	Bal.	-	-	-	[33]
Nickel B	-	-	-	-	-	Bal.	-	-	-	[34]
Nickel C	-	-	-	-	-	Bal.	-	-	-	[9]

Table 3: Geometry of the samples tested in this work.

Steel	Geometry	w (mm)	h (mm)	R (mm)	L (mm)
Ferritic A	Cylindrical	-	-	10	0.1
Ferritic B	Cylindrical	-	-	2.5	5
Ferritic C	Plate	1	12.6	-	12
Ferritic D	Cylindrical	-	-	4	15
Martensitic A	Cylindrical	-	-	20	1.1
Martensitic B	Cylindrical	-	-	2.5	25
Mart/Pearl (Mart)	Cylindrical	-	-	7.5	-
Mart/Pearl (Pearl)	Cylindrical	-	-	3.25	-
Pearlitic A	Cylindrical	-	-	2.5	20
Pearlitic B	Plate	5	5	0	5
100Cr6	Cylindrical	-	-	4	2
100Cr6+0.5V	Cylindrical	-	-	4	2
100CrMnMoSi8-4-6	Cylindrical	-	-	4.25	8.8
TWIP	Cylindrical	-	-	10	1.4
AISI 310	Plate	1	4.8	-	5
Nickel A	Cylindrical	-	-	20	0.1
Nickel B	Plate	-	-	-	0.18
Nickel C	Plate	-	-	-	0.35

6.1 Sample preparation, charging conditions and thermal desorption analysis in 100Cr6 series

100Cr6, 100Cr6+0.5V and 100CrMnMoSi8-4-6 casts were spheroidised to improve machinability, following the schedule outlined in [55]. Both 100Cr6 and 100Cr6+0.5V specimens were cut into cylindrical dilatometry samples (8 mm diameter and 12 mm long) and heat treated in vacuum in a Thermecmaster dilatometer with helium quenching gas at a cooling rate of 25 °C/s. 100Cr6 and 100Cr6+0.5V casts were treated according to the schedules

designed by Szost *et al.* [23], respectively. After heat treatment each sample was reduced to a coin—shape geometry (Table 3). 100CrMnMoSi8-4-6 samples were treated according to the schedule outlined in [56]: they were heated to 885 °C for 20 minutes in salt, then quenched to 235 °C and held for 14 hours, at the end they were left to cool on air at room temperature, then washed. After heat treatment, 100CrMnMoSi8-4-6 samples were cut into rods (Table 3).

Hydrogen charging was performed at different times in a cathodic electrolysis process. The hydrogen charging cell is a galvanic cell consisting of an anode and surrounded by a platinum counter electrode wire which serves as cathode, both are submerged in a water-based electrolyte of 3 wt% NaCl + 0.3 wt% NH_4 SCN (ammonium thiocyanate). During the charging process, an electrical current is applied between the anode and the cathode with a current density 1 mA cm^{-2}, which causes the water in the electrolyte to break down, releasing oxygen gas at the anode and hydrogen gas at the cathode. After being separated, the electrolyte is purged from oxygen by nitrogen or argon gas produced into the cell to prevent the reaction between the two gasses. After hydrogen charging, the samples were cleaned with IMS (Industrial Methylated Spirits), surface re-polished using 2500 grit SiC paper to remove the oxide layer, rinsed with isopropanol, then dried. The specimens were left at room temperature for degassing before testing in TDS, then heated inside the TDS furnace tube to measure the trapped H escaping during the heating. As heating proceeds, hydrogen is released and mixed with the carrier gas (helium) that flows continuously through all the system at a flow rate of 10 ml/min. The sample gas was analysed at 3 minutes intervals. Hydrogen is released continuously from the sample with time at a heating rate of 100 °C/h. During the test the steel sample is heated from room temperature to approximately 400 °C. The measurements were performed with Agilent Technologies 7890B GC system.

6.2 Determination of the microstructure

A number of microstructural features were obtained directly from experimental characterisation, including grain size, as well as particle fraction and mean radius. For 100Cr6

and 100Cr6+0.5V the microstructure has been previously characterised in [23], and for 100CrMnMoSi8-4-6 in [56]. For the case of Martensitic B, since this alloy has carbides with mixed elements (Mo and V), f_p and r_p are taken from the estimations by Yamasaki and Bhadeshida [42] for a tempered steel with similar Mo and V content. Additionally, M_2C carbides are rod–shaped, and an effective radius is considered to estimate N_p: $r_{eq} = \sqrt{\frac{2r_p L_p}{\pi}}$, where L_p is the particle length. An aspect ratio of $\frac{L_p}{d_p} = 5$ is considered based on experimental observations [42].

The dislocation density was not reported in various cases and different methods were employed to estimate ρ based on the specific material's processing conditions. For the case of ferritic steels, ρ was estimated using Taylor's equation: $\sigma = \sigma_Y + 0.25 M \mu b \sqrt{\rho}$, where σ is the flow stress at the given strain, σ_Y is the yield stress, $M = 3$ is the Taylor orientation factor, $\mu = 80$ GPa is the shear modulus and $b = 0.285$ nm is the Burgers vector. Ferritic A and D were 40 % and 50 % cold-rolled, respectively, however σ values were not reported. $\sigma = 375$ MPa and $\sigma = 500$ MPa for A and C, respectively, were estimated from [57]. For Ferritic B, Vickers hardness values from uniaxial tensile tests (at strains up 25 %) were transformed into flow stress $H_v = \frac{1}{3}\sigma$ (including σ_Y for $\varepsilon = 0$). ρ in Ferritic C was obtained from uniaxial compression tests (reported in [16]) at $\varepsilon = 10$ % and 20 %.

The dislocation density for martensitic steels (Martensitic B, Mart/Pearl, 100Cr6 and 100Cr6+0.5V) was calculated using a model previously defined by the authors [58,59]. It includes the effects of carbon content and tempering conditions in ρ and it can be applied to the steels tested in this work. Details on the calculations can be obtained from [58,59]. Tempering conditions for each steel were reported in the referring article. ρ in Martensitic A was obtained from [22]. For the case of 100CrMnMoSi8-4-6, ρ was assumed based on typical values for bainitic steels [60]. ρ in pearlitic steels has been estimated by Guo *et al.* [61] to lie in the range $10^{14} - 10^{15}$ m^{-2}; the values shown for Mart/Pearl (in pearlitic form), Pearlitic A and Pearlitic C, were assumed based on their relative yield stress values: 1400 [17], 1838 [18] and 1192 MPa [44], respectively. ρ in Nickel A was considered low, since they its previously annealed, whereas for Nickel C, the dislocation density of a 90

% cold–rolled specimen was considered [57]; no grain size was reported. Different grain sizes were tested in Nickel B [34].

For pearlitic steels, since the cementite lamellae boundaries dictate the hydrogen diffusion rate [46], N_t/N_l in equation 14 is considered the same as for grain boundaries: $\frac{N_{Fe_3C}}{N_l} = \frac{b}{\Lambda_{Fe3C}}$, where Λ_{Fe3C} is the mean lamellar spacing; these values are shown in Table 4 as r_θ, and are estimated from [18].

Table 4: Microstructures of the materials tested in this work.

Steel	ρ (m^{-2})	D_g (μm)	f_θ (%)	r_θ (nm)	f_p (%)	r_p (nm)	Carbide
Ferritic A	2.5×10^{14}	-	-	-	-	-	-
Ferritic B	$1.8 \times 10^{13} - 1.8 \times 10^{14}$	-	-	-	-	-	-
Ferritic C	$7.6 - 13.6 \times 10^{13}$	130	-	-	-	-	-
Ferritic D	1.5×10^{15}	-	-	-	-	-	-
Martensitic A	3.25×10^{14}	-	-	-	1.2	30	M$_2$C
Martensitic B	5.5×10^{14}	8	4	20	0.5	10	M$_4$C$_3$
Mart/Pearl (Mart)	3.4×10^{14}	15	10	10	-	-	
Mart/Pearl (Pearl)	3×10^{14}	15	-	75(*)	-	-	
Pearlitic A	6×10^{14}	20	-	75(*)	-	-	
Pearlitic B	2×10^{14}	20	-	75(*)	-	-	
100Cr6	9.8×10^{15}	20	10	10	-	-	-
100Cr6+0.5V	9.8×10^{15}	20	10	10	0.9	5	M$_4$C$_3$
100CrMnMoSi8-4-6	5×10^{14}	20	10	25	-	-	-
TWIP	10^{10}	10	-	-	-	-	-
AISI 310	10^{10}	-	-	-	-	-	-
AISI 301	$6 \times 10^{13}(\gamma)$, $6 \times 10^{14}(\alpha')$,	-	-	-	-	-	
Nickel A	10^{11}	10	-	-	-	-	-
Nickel B	-	0.12-168	-	-	-	-	-
Nickel C	10^{15}	-	-	-	-	-	-

7   Results

In order to compare the model results with experiments, we consider the hydrogen concentration at the centre of the specimen ($z = r = 0$ in equation 7 or $x = y = z = 0$ in equation 22), where diffusion is slowest. This ensures hydrogen transport is fully active throughout the specimen, providing more accurate estimations of the diffusion profiles. The lattice diffusion parameters in $\alpha(\alpha')$–Fe are equal to [62]: $D_0 = 1.1 \times 10^{-7}$ m^2/s and $Q = 6.7$ kJ/mol; for γ–Fe the diffusion parameters for AISI301 are [54]: $D_0 = 5 \times 10^{-7}$ m^2/s and $Q = 48.8$ kJ/mol. These values were considered constant in other austenitic steels. The lattice diffusion parameters for nickel are [9]: $D_0 = 7.5 \times 10^{-7}$ m^2/s and $Q = 39.1$ kJ/mol.

It is interesting noting that the three models are tested simultaneously in several alloys, since permeation and degassing provide initial concentration for thermal desorption analysis. Table 5 shows the charging conditions for the materials tested, as well as the n_0 values adjusted. It is worth noting that n_0 was constant for a given charging electrochemical solution, although these values might differ in other materials. Gas pressure permeation tests were conducted in TWIP, Nickel A and C, and n_0 and $D_{perm,0}$ were adjusted to match the experimental data; this is to allow us to evaluate temperature effects in the permeation profiles. No information on charging conditions for thermal desorption tests were reported for Nickel C and $c_{0,desorp}$ were adjusted to the experimental desorption analysis. Ferritic D was charged by gas pressure, however this value is not necessary to estimate, since only the peak temperature for different heating rates is employed. I_c was not reported for Pearlitic A and 1 A m^{-2} was assumed in the calculations. Similarly for Pearlitic B no charging conditions were provided and the initial concentration was adjusted to match the experimental data. For AISI 310, the current density was approximated using the cathodic overpotential reported in [53] with the estimation of I_c reported by Wu [5].

Table 5: Charging and desorption conditions of the materials tested in this work.

Steel	I (A/m^2)	t_{charg} (h)	ϕ (°C/h)	t_{degas} (h)	Solution	n_0 (wppm A$^{-1/2}$ m)
Ferritic A	1-10	1	-	-	0.1N NaOH	9.4×10^7
Ferritic B	5	-	-	-	3%NaCl+0.3%NH$_4$SCN	4.7×10^8
Ferritic C	1	12	100	0.25	3%NaCl+0.3%NH$_4$SCN	4.7×10^8
Martensitic A	200	5	-	6	1M H$_2$SO$_4$	–
Martensitic B	100	100	-	200	0.1N NaOH	9.4×10^7
Mart/Pearl	10	48	100	-	0.1N NaOH+	4.7×10^8
					3%NaCl+0.3%NH$_4$SCN	
Pearlitic A	-	24–120	100	-	0.2M NH$_4$SCN	7.5×10^8
100Cr6	10	24	100	72	3%NaCl+0.3%NH$_4$SCN	4.7×10^8
100Cr6+0.5V	10	24	100	24	3%NaCl+0.3%NH$_4$SCN	4.7×10^8
100CrMnMoSi8-4-6	10	48, 72	100	168	3%NaCl+0.3%NH$_4$SCN	4.7×10^8
AISI 310	1	60	360	-	1N H$_2$SO$_4$+0.002%CH$_2$N$_2$S	9.2×10^{19}
Nickel B	200	0.16-0.5	-	0.16-0.4	-	-

Figure 3 shows the effect of charging conditions, microstructure and sample geometry during permeation in steels. Figure 3(a) shows the model results of the steady state permeation density I_∞ in Ferritic A for different charging current densities. In order to obtain the evolution with time the relationship is used [22]: $I_\infty = \kappa_c c_{charg}$, with $\kappa_c = 35$ μA cm^{-2} wppm^{-1}. The model results show good agreement for the steady state values and transient values at higher charging densities ($I_c \geq 1$ A m^{-2}); however, the lag time before reaching steady state is underpredicted by ~ 15 minutes for $I_c = 1$ A m^{-2}. This can be due to the thickness of the sample being too low, since the oxide layer forming at the surface has stronger influence in the permeation rate in very thin sheets [28]. Figure 3(b) shows a comparison between the normalised permeation (blue) and degassing (red) profiles in Martensitic A. The model shows very good agreement for the permeation curves, however it shows slower kinetics for starting degassing, although it predicts correctly the time for J_∞ to be null. This can be due to trapped H atoms being released and trapped again as the number density of trapping sites is very high; this effect is not explicitly captured by the model. In order to validate the relationship between the hydrogen trapped on dislocations

(equation 14), Figure 3(c) shows the hydrogen concentration values as function of the increase in the dislocation density in cold–rolled Ferritic B, where the model is able to reproduce the increase in concentration with increasing the dislocation density; uniaxial tensile tests were performed to increase ρ and the sample surface area changes as the length increases: $L = L_0(1 + \varepsilon)$, where L_0 is given in table 3 and $\varepsilon \leq 0.25$ [51]. Figure 3(d) shows a parametric analysis on the effect of the sample radius to reach steady state permeation (and trap saturation) in a ferritic sample with $\rho = 2.5 \times 10^{14}$ m^{-2}. It can be observed that thick samples ($R = 10$ mm) contain more hydrogen due to the increase in surface area, however full saturation (steady state) is not fully reached after 1000 hours. Conversely, thin samples ($R = 1$ mm) contain less hydrogen and steady state is reached in less than 50 hours.
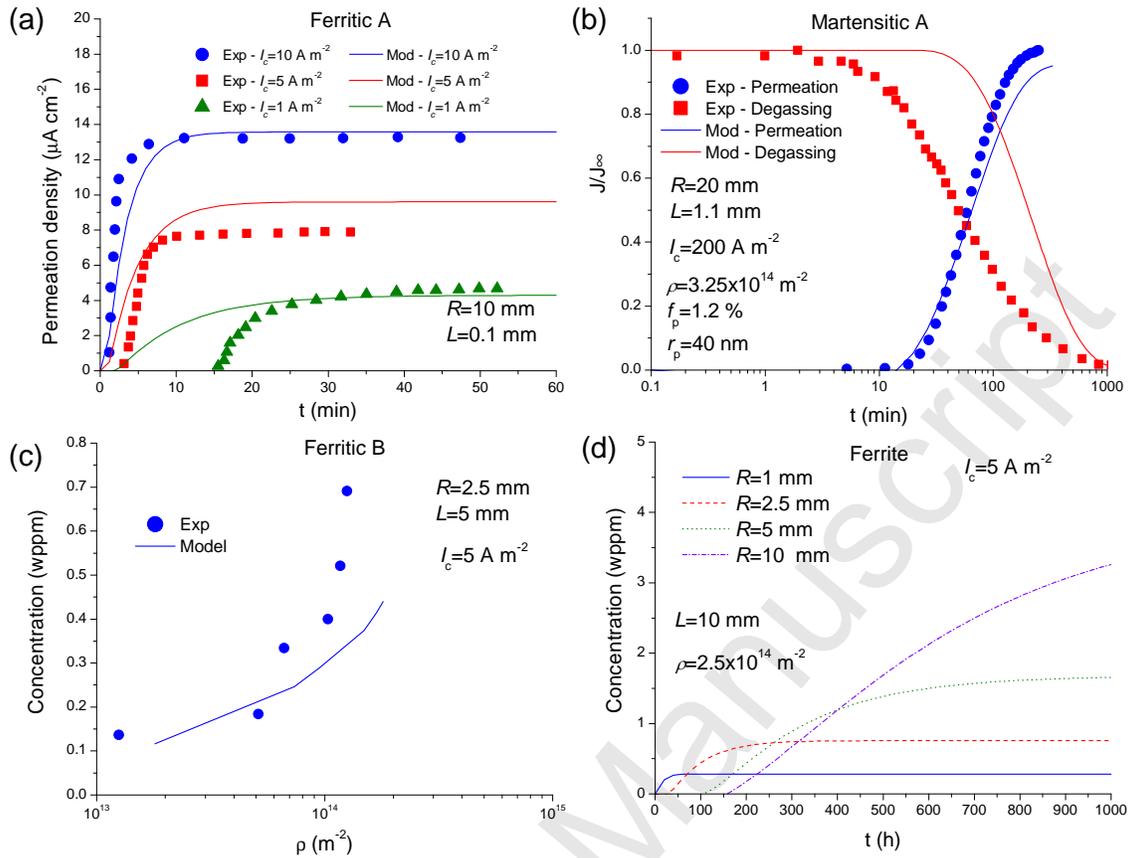
23

Figure 3: (a) Effect of the charging density in the permeation profile of cold-rolled Ferritic A. (b) Permeation/degassing profile in Martensitic A. (c) Hydrogen concentration as function of the dislocation density in Ferritic B. (d) Effect of the sample radius in the time for saturation and hydrogen concentration in deformed ferrite.

Figure 4(a) shows the concentration profile of Pearlitic A during electrochemical charging, where dislocations and cementite lamellae are considered as trapping sites. The model shows good agreement with the experimental data for both individual and total concentrations. It is shown that the traps in the cementite lamellae saturate very quickly, whereas for dislocations it takes more than 100 hours to fully saturate. Figure 4(b) shows the degassing profile in Pearlitic B, where the model again shows very good agreement with the experiments. It is interesting noting that the degassed hydrogen is released mostly by dislocations (red curve), whereas the concentration of hydrogen in the cementite (green curve) remains practically constant. This shows that for pearlitic steels the cementite lamellar are efficient trapping sites as the hydrogen can remain trapped for long time

(more than 1000 hours). Figure 4(c) shows the permeation and degassing profiles of Martensitic B, where multiple trap species are present; the model shows good agreement with the experiments in both conditions. The main concentration drop is due to de-trapping on dislocations. Figure 4(d) shows the relative contribution to the hydrogen concentration in the sample, where most of the hydrogen is trapped at the dislocations. It is also interesting noting that dislocations also dictate the time for saturation, as the precipitates saturate quickly. These results show that dislocations have a strong influence in the overall hydrogen transport process, as they take longer time to saturate during permeation and are released quickly during degassing.
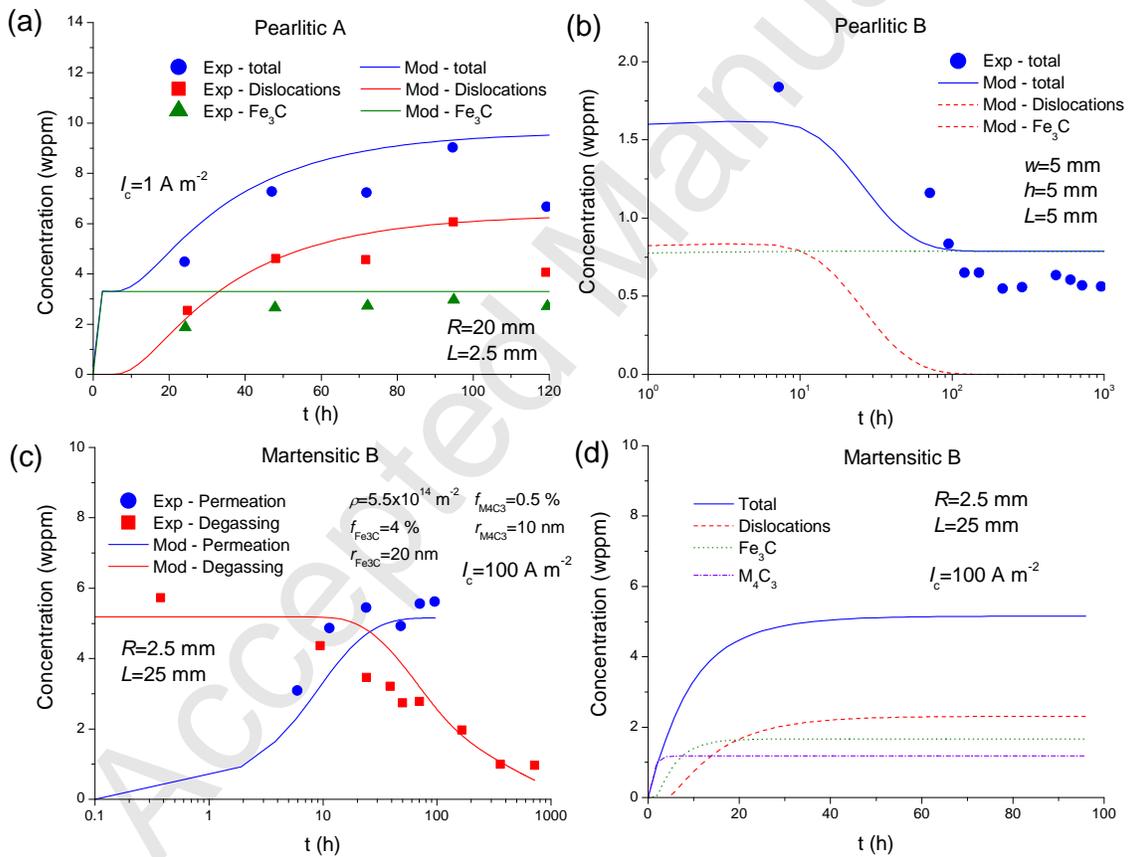

Figure 4: (a) Charging and (b) degassing profiles in pearlite. (c) Charging/degassing profiles in Martensitic B and (d) the relative contribution of various microstructural features to the total concentration.

Figure 5 shows the effects of different microstructural features on electrochemical charging and thermal desorption spectroscopy in steels; the former dictates the height of

the peaks in the desorption plots (Table 5). Figure 5(a) shows the model and experimental results in Ferritic C containing different dislocation densities showing good predictions in the temperature range and heigh of the peaks. In Figure 5(b), desorption results are shown in Mart/Pearl in both martenstitic (blue) and pearlitic (red) form; the first peak in pearlite is due to dislocations, whereas the second peak is due to lamellae of cementite. In both cases the model shows good agreement with the experimental results in the temperature range and heigh of the peaks in Pearl, however, lower height is predicted in Mart; this could be due to a different number density of traps being present in the material (Table 4). Figure 5(c) shows the model results in Pearlitic A for different charging times; the model shows good results in the first peak (dislocations) for $t_{charg} = 72$ h and 96 h, however it shows much lower concentration for $t_{charg} = 24$ h. For the case of the second peak the model predicts a peak temperature of 250 °C, whereas the experiments show peak temperatures at 350 °C, however a second peak is also measured at $250 - 275$ °C. Although the nature of this behaviour was not identified in [18], when comparing these results with additional measurements in the same material and with Mart/Pearl (pearlite), no two–step peaks were measured. This suggests that the spread in the peaks could correspond different lamellae alignments and slowing down the detrapping rate [46]; nevertheless, the total concentration in the peak is well reproduced (Figure 4(a)). Figure 5(d) shows the effects of the heating rate in the peak temperature in cold–drawn Ferritic D, where the model is able to capture the variation rate in the peak temperature with ϕ. However, it shows lower values by 40-50 K. This can be due to a different dislocation density being present in the material (Table 4).
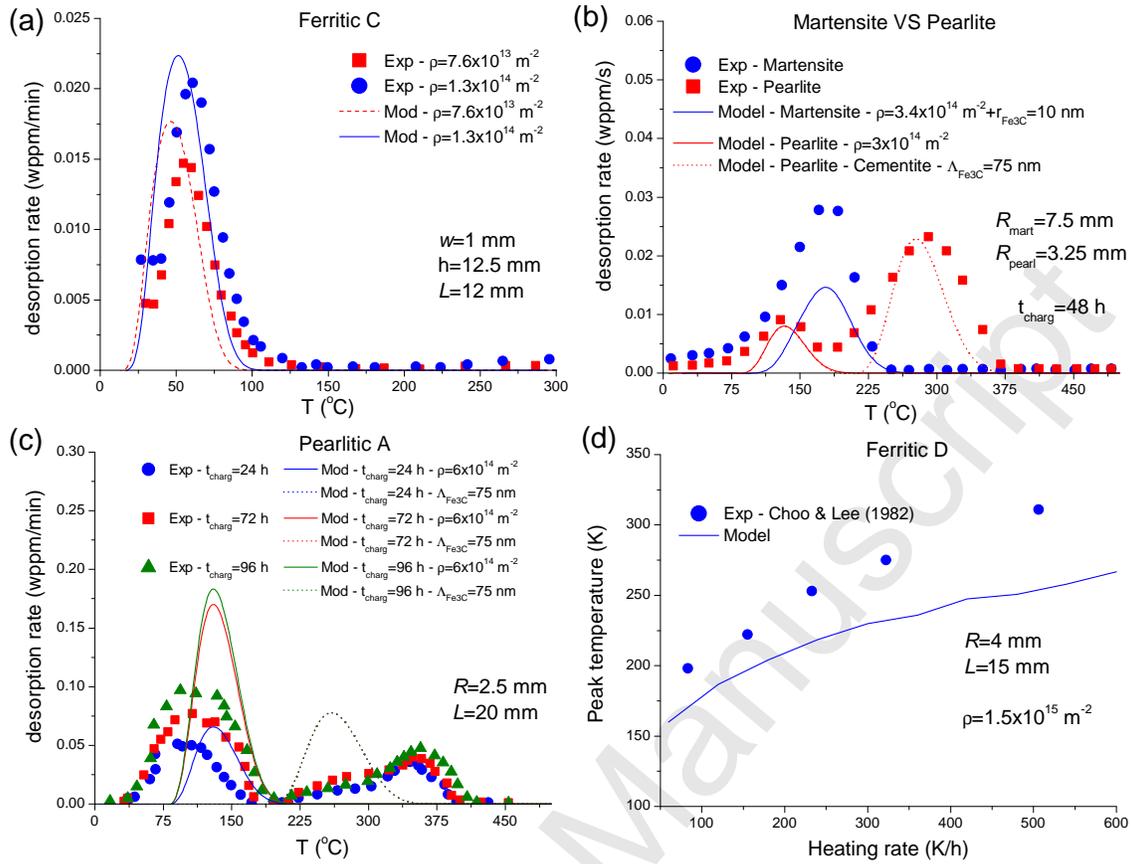
Figure 5: (a) Thermal desorption results in Ferritic C for various dislocation densities. (b) Comparison in the desorption profiles between martensite and pearlite in Mart/Pearl. (c) Effect of charging time in the desorption profiles in a Pearlitic A. (d) Variation in the peak temperature as function of the heating rate in Ferritic D.

Figure 6 shows the model results for 100CrMnMoSi8-4-6, including (a) thermal desorption, (b) concentration profile and (c) degassing before desorption after 48 and 72 hours of electrochemical charging. The model shows good results in the peak temperatures, however it predicts higher peaks and narrower spread the desorption rate than the experimental results. This can be due to the fact that this high–carbon steel contains a very high dislocation density that may alter the interactions between hydrogen and the total number of trapping sites and the linear summation of the concentration of different trapping species might no longer hold. This is shown by predicting that dislocations strongly influence the hydrogen concentration during charging (b) and degassing (c), as the concentration in cementite does not decrease much. Additionally, the assumption of

describing diffusion at the centre of the sample might not be sufficient due to the slow diffusion and a different estimation could be adopted. Nevertheless, the total concentration of hydrogen estimated from TDS lies in the same range (Figure 6(c)). Figure 6(d) shows the effect of vanadium in 100Cr6 martensitic steel series, where more hydrogen is trapped on 100Cr6+0.5V (red) due to the higher number density of strong carbides, than in the base alloy (blue). In both cases the model describes well the experimental measurements. It is worth noting that for the case of 100Cr6, most of the hydrogen has been released from the dislocations (green dashed lines are practically null) due to the degassing step and the remaining concentration is due to hydrogen being trapped at the cementite, where the solid blue (total) and orange dotted (Fe$_3$C) overlap.
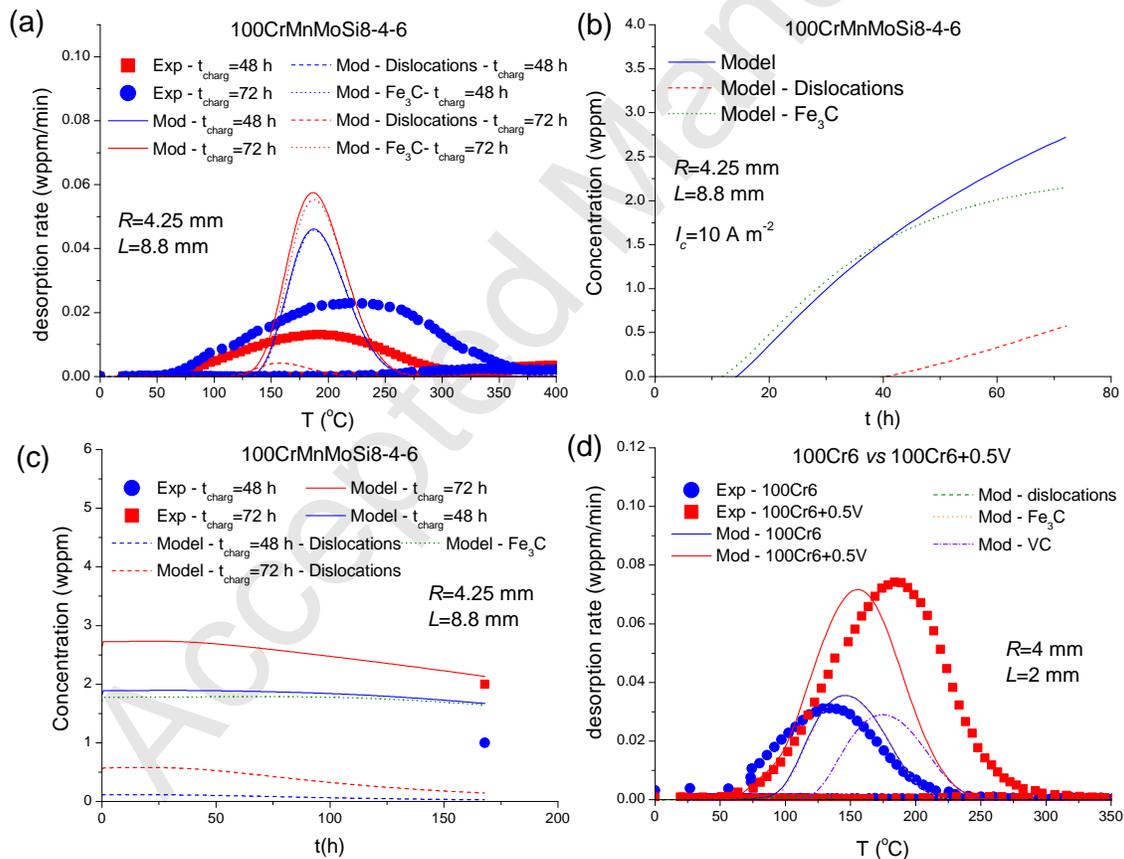

Figure 6: (a) Thermal desorption spectroscopy in 100CrMnMoSi8-4-6. Predicted concentration profile during charging (b) and (c) degassing prior the desorption tests. (d) Effect of vanadium in 100Cr6 series.

Figure 7 shows the model application to austenitic steels. Mass flow rate curves

during permeation in TWIP are shown in (a) and compared against experimental measurements under various charging temperatures; the permeation density is estimated as $J_\infty = \kappa_{TWIP} c_{perm}$, where $\kappa_{TWIP} c_{perm,0} = 8.9 \times 10^{11}$ mol m^{-2} s^{-1}. The model shows very good agreement with the experimental results for different temperatures. In Figures 7(b) and (c), results are shown in AISI310 for hydrogen concentration during charging and thermal desorption curves, respectively. The model shows good results in the former, whereas for the desorption curves it shows a difference in the peak temperature of up to 80 °C; this can be due to the presence of different microstructural features or due to variations in the lattice diffusion parameters of this alloy [4]. Figure 7(d) shows the variation in the diffusion coefficient with the volume fraction of transformation–induced martensite in the metastable steel AISI 301. D is estimated as the effective coefficient in a dual–phase alloy [54]: $\frac{f(P_{eff} - P_{\alpha'})}{P_{eff} - 0.5P_{\alpha'}} + \frac{(1-f)(P_{eff} - P_\gamma)}{P_{eff} - 0.5P_\gamma} = 0$, where $P_{eff} = D^{-1/2}$, $P_{\alpha'} = D_{\alpha'}^{-1/2}$ and $P_\gamma = D_\gamma^{-1/2}$. The upper and lower dotted lines denote the values of $D_{\alpha'}$ and D_γ at 320 °C, respectively; these were obtained using equation 1 and the dislocation densities shown in Table 4. The model shows very good agreement with the experimental data, demonstrating that it can capture hydrogen kinetics both in austenitic and martensitic form, as well as for intermediate configurations.
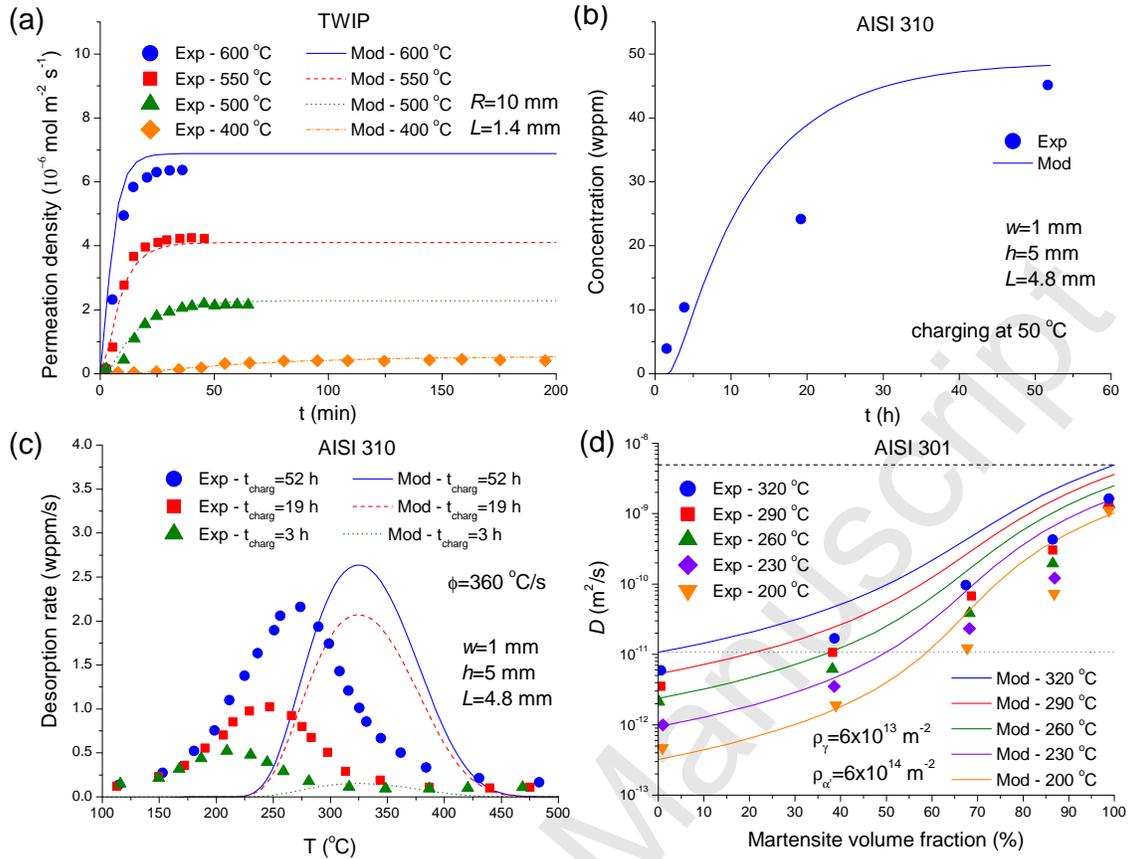
Figure 7: Hydrogen transport in austenitic steels: (a) Permeation when charging at various temperatures in a TWIP steel. (b) Concentration profile during charging and (c) thermal desorption results in AISI 310. (d) Variation in the diffusion coefficient of AISI 301 as function on the martensite volume fraction.

Figure 8 shows the model results and comparison with experimental data in polycrystalline nickel. Figure 8(a) shows the permeation and degassing profiles in Nickel A, whereas Figure 8(b) and (c) show respectively the permeation profiles and permeation coefficient in Nickel B for various grain sizes. The model shows very good agreement with the experimental data, demonstrating that the higher number density of traps accelerates diffusion during permeation. Figure 8(d) shows the effects of the sample thickness in the desorption profiles of Nickel C, where the model predicts the variations in L on the peak temperatures; however, it shows narrower desorption curves. This can be due to slower diffusion kinetics increase the spread of interactions of hydrogen atoms with traps, and the releasing/re–trapping events become more significant to the desorption rate.
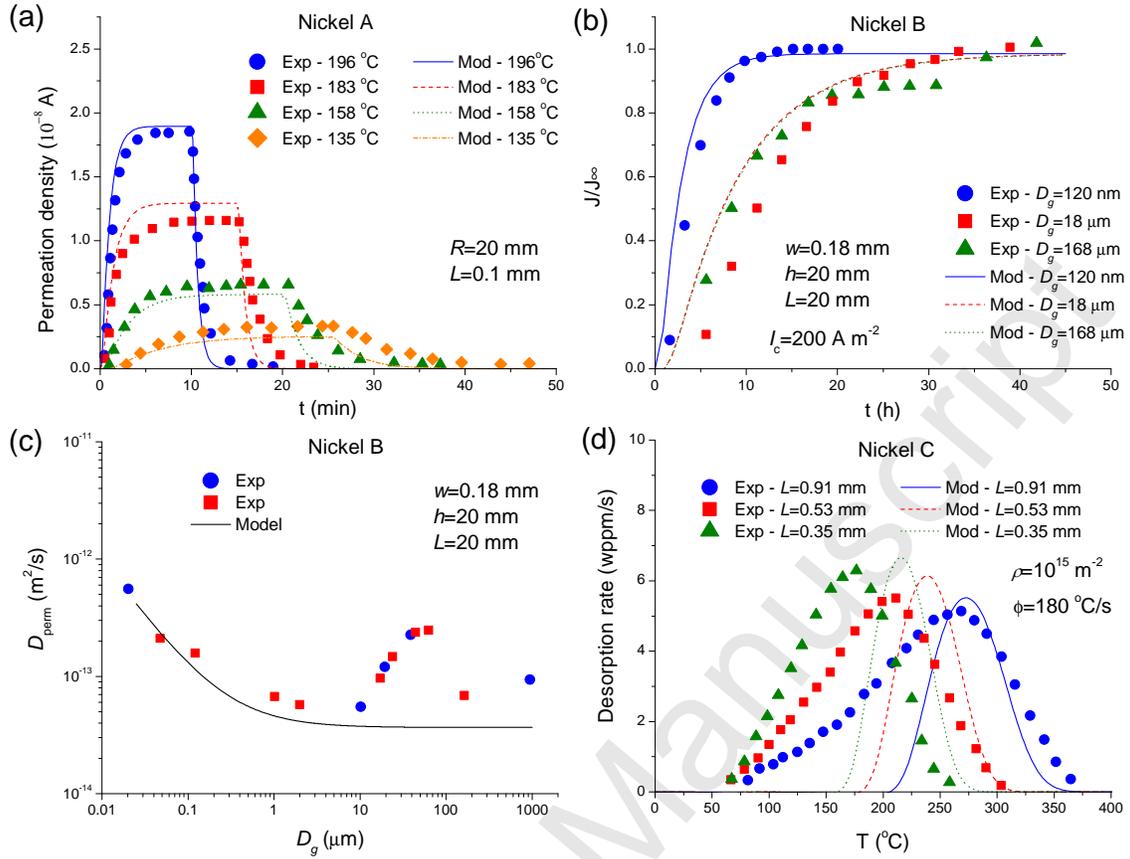
Figure 8: Hydrogen transport in pure nickel: (a) Permeation/degassing at various temperatures in Nickel A; (b) current density saturation profiles for various grain sizes in Nickel B; (c) variation in the effective diffusion coefficient during permeation as function of the grain size. (d) Thermal desorption results for various sample thicknesses in Nickel C.

8 Discussion

A unified modelling framework for describing hydrogen transport during electrochemical permeation, degassing and thermal desorption spectroscopy has been proposed. The methodology includes relevant features such as electrochemical charging conditions, three–dimensional geometry, and a direct link between the trapping parameters and microstructural features. The diffusion profiles during permeation were obtained by including the increase in the energy barrier for diffusion due the formation of an oxide layer at the surface and a diffusion term from the electrochemical charging process accelerating mass

transport. The effect of charging parameters on hydrogen permeation has been studied previously by a number of authors [4, 5, 26, 27]. It has been observed that the apparent diffusivity during permeation D_{perm} not only depends on the microstructure but also on the square root of the charging current density $I_c^{1/2}$ [8, 22]. It was shown by the current model that this is due to the increase in charging current increasing the electric charge passing through the sample and accelerating the diffusion process. The models for degassing and thermal desorption were described by estimating the rate at which trapping wells release hydrogen atoms into the lattice and the environment under homogeneous diffusion.

The number density of traps was found to be proportional to the linear spacing of the respective microstructural feature. This is due to the diffusion paths of hydrogen atoms follow a line (in a 3-D space) and the probability for an atom to encounter a trap is dictated by the mean free path of the crystal defect [32]. This allowed us to apply the model to different steels using the same binding energies and trapping parameters in the three scenarios of permeation, degassing and desorption. Although two parameters were adjusted, κ and n_0, the former was constant for all steels tested that were not austenitic; κ holds the same values for distinct austenitic steels. Similarly, n_0 was shown to depend only on the electrochemical solution employed for charging each sample, although it might also depend on the crystal structure. This shows that these parameters only depend on the experimental setup of eletrochemical charging and are independent on the microstructure and sample geometry. For materials with a high number density of traps, the models for thermal desorption were successful in predicting the peak temperatures, however they failed to fully predict the desorption profiles. This was due to Fickian diffusion not accounting for interaction between traps. Nevertheless, the methodology is satisfactory in identifying trapping effects during permeation, degassing and thermal desorption and can be conceived as a tool for process and microstructural design to prevent hydrogen embrittlement.

8.1 Modelling hydrogen transport: Classical approximations

An interesting aspect to explore is how the present approach compares with classical approximations. For instance, equation 12 can be compared with Kissinger equation applied to TDS [11]:

$$\frac{dx_K}{dt} = A_{Kiss}(1 - x)^m \exp\left(-\frac{Q + E_b}{R_{gas}T}\right),$$ (17)

where x_K is the fraction of hydrogen released at a given time; $Q + E_b$ is the trap activation energy, and m and A_{Kiss} are fitting constants. $Q + E_b$ is related to the peak temperature T_c (maximum desorption rate) via the relation:

$$\frac{d\left(\ln\left(\frac{\phi}{T_c^2}\right)\right)}{d\left(T_c^{-1}\right)} = -\frac{Q + E_b}{R}$$ (18)

where ϕ is the heating rate. Although this relationship has been widely applied to estimate E_b from TDS experiments [17–19], the peak temperature T_c in fact depends on A_{Kiss} and m [11]:

$$\frac{(Q + E_b)\phi}{R_{gas}T_c^2} = A_{Kiss}n(1 - x)^{m-1}\exp\left(-\frac{Q + E_b}{R_{gas}T_c}\right).$$ (19)

This implies that equation 18 can only be used to estimate the binding energy if A_{kiss} and m are known. Moreover, no information on the dimensions and microstructure are included in this analysis.

Using the model introduced in this work and defining the variable $x_{mn} = 1 - \frac{c_{desorp,mn}}{c_{0,desorp}}$, where $c_{desorp,mn} = c_{0,desorp}\exp(-D(\lambda_n^2 + \alpha_m^2)t)R_nZ_m$ is the $m, n-$eigenfunction of c_{desorp}; x_{mn} represents the fraction of hydrogen released at a given time by the m, n term in equation 11. In order to simplify the analysis, it is assumed that $\frac{N_t}{N_l}\exp\left(\frac{E_b}{R_{gas}T}\right) \gg 1$,

hence the term $(D + \frac{dD}{dt}t) \sim D_0 \frac{N_l}{N_t} \exp\left(-\frac{Q+E_b}{R_{gas}T}\right)$. Differentiating x_{mn} with t it gives:

$$
\begin{aligned}
\frac{dx_{mn}}{dt} &= \left(D + \frac{dD}{dt}t\right)(\lambda_n^2 + \alpha_m^2)\exp(-D(\lambda_n^2 + \alpha_m^2)t)R_n Z_m \\
&\approx D_0 \frac{N_l}{N_t}\exp\left(-\frac{Q+E_b}{R_{gas}T}\right)(\lambda_n^2 + \alpha_m^2)(1 - x_{mn}) \\
&= A_{mn}(1 - x_{mn})\exp\left(-\frac{Q+E_b}{R_{gas}T}\right),
\end{aligned}
\tag{20}
$$

where $A_{mn} = D_0 \frac{N_t}{N_l}(\lambda_n^2 + \alpha_m^2)$. This result shows that the Kissinger equation (17) is virtually reproduced by using Fickian diffusion. Moreover, the effects of sample geometry and microstructure are explicitly described in the rate factor A_{mn}.

Another important approach typically employed for hydrogen transport was introduced by McNabb and Foster [12]. They proposed a modified diffusion equation for trapped hydrogen:

$$
\frac{\partial \theta_t}{\partial t} = k_{MF}c_L(1 - \theta_t) - p_{MF}\theta_t,
\tag{21}
$$

where N_t is the number of trapping sites per unit volume, $\theta_t = c_t/N_t$ is the trapping occupancy, and $k_{MF} = k_0 D_0 \exp\left(-\frac{Q}{R_{gas}T}\right)$ and $p_{MF} = p_0 \exp\left(-\frac{Q+E_b}{R_{gas}T}\right)$ are the rate of capture and escape per trap, respectively. This equation aims to describe the rate at which hydrogen in the lattice enters into the trapping wells. If the concentration in the lattice does not vary much, the previous equation has the same form than equation 6 (under separation of variables), where the rate of concentration of hydrogen in the traps decreases as the traps are saturated ($\theta_t \sim 1$) and the solution of θ_t increases exponentially in time according to the rate $-(k_{MF}c_L + p_{MF})$; all the models found in our approach follow an exponential variation in t. These results show that the models proposed in this work are consistent with classical approaches for hydrogen transport.

8.2 Parametric analysis in martensitic steels

Martensitic steels are highly prone to embrittlement from hydrogen atoms located in the lattice [63]. In the context of hydrogen diffusion, it is interesting to study the effects of distinct microstructural features affecting hydrogen transport in these steels, since hy-

drogen mobility can vary substantially depending on the carbon content and tempering conditions of the steel [58, 59]. Figure 9 shows hydrogen concentration and transport during permeation, degassing and desorption in steels with different dislocation densities and particle sizes, where Fe_3C and vanadium carbides (M_4C_3) are considered. Figure 9(a) and (b) show the variation in the concentration of trapped hydrogen and diffusion coefficient on each trap, respectively. $3\%NaCl+0.3\%NH_4SCN$ solution and $I_c = 10$ A m^{-2} are considered in a cylindrical specimen with $R = 2$ mm and $L = 10$ mm. Dislocations trap most of the hydrogen if the particles have a radius larger than 40 nm. Moreover, the diffusion coefficient in these steels is largely controlled by dislocations since they display the highest values for very wide ranges of ρ if $r_p \geq 50$ nm. The diffusion coefficients experimentally estimated in martensite are in the range of $10^{-10} - 10^{-12}$ m^2/s [22, 45], which correspond to the diffusion coefficient (Figure 9(b)) of hydrogen trapped at dislocations ($\rho = 10^{14} - 10^{16}$ m^{-2}). Similarly, Figure 9(c) shows the variation of the apparent diffusion coefficient during permeation, where D_{perm} is controlled by the variation in ρ due to the slower trapping rate delaying steady state. By comparing the diffusion profiles it is evident that vanadium carbides are effective trapping sites, since the will slow down diffusion during degassing (Fig. 9(b)) and trap hydrogen rapidly during charging (Fig. 9(c)). Figure 9(d) shows the variation in peak temperature during desorption where it shifts to higher values as the trapping density increases. For instance a steel with $\rho = 6 \times 10^{14}$ m^{-2} and $r_{Fe_3C} = 40$ nm will show a single peak. This is consistent with experimental results found in 100CrMnMoSi8-4-6 and 100Cr6 series, where a single peak was found to be the summation of hydrogen trapped at dislocations and cementite. More importantly, this also shows that high–strength steels will display peaks at higher temperatures due to the high number density of traps, hence avoiding the need of fitting very high trapping energies [24].

These results show that hydrogen mobility in martensitic steels can be strongly controlled by dislocations, as they can release hydrogen to the lattice more rapidly than other kinds of traps due to their low binding energy (Table 1) and can accumulate a high fraction of the hydrogen content in the steels. These combined effects can contribute to the in-

creased susceptibility for hydrogen embrittlement in martensitic and other high–strength steels, via increasing the concentration of hydrogen in the lattice during plastic deformation when dislocations release them [64]. Nevertheless, the introduction of stronger traps, such as vanadium carbides, can help to counteract this effect by strongly trapping the released hydrogen in the lattice [23]. These results can be combined with models for mechanical properties to design hydrogen–resistant steels.
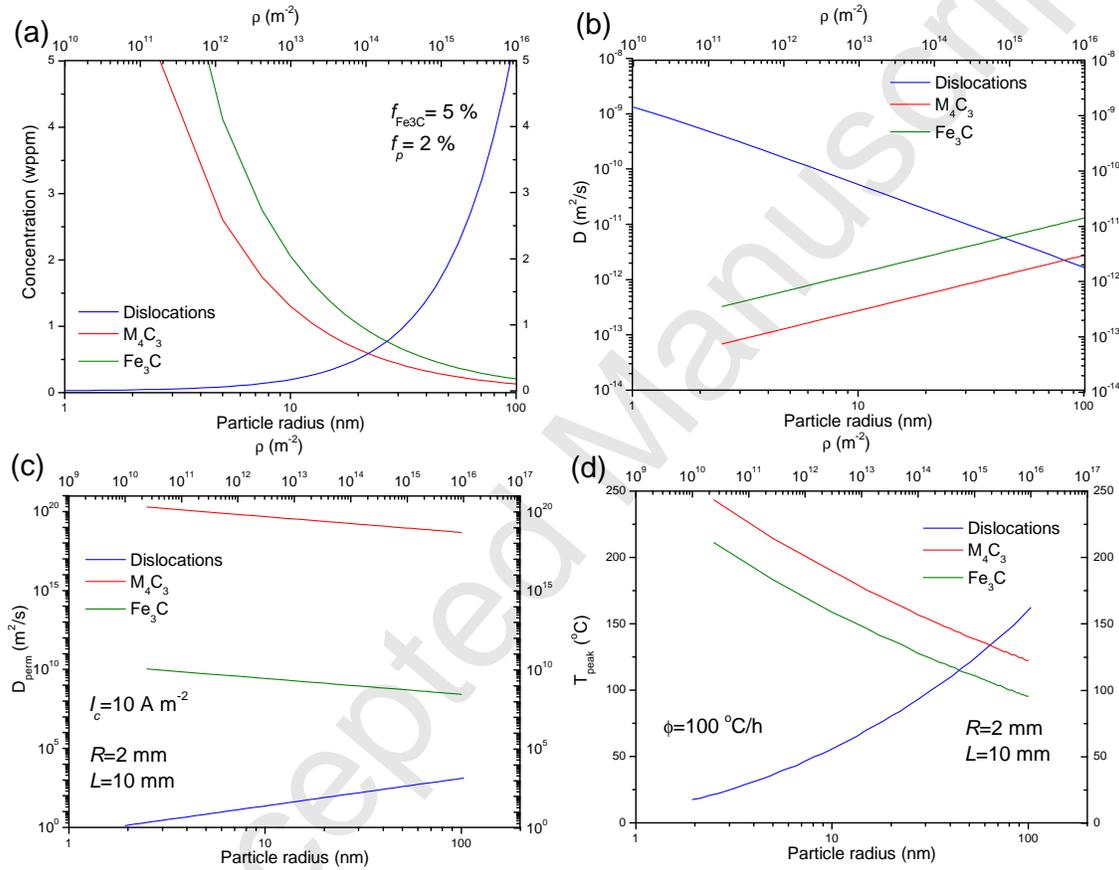

Figure 9: Parametric analysis in martensitic steels: effect of dislocations, cementite and vanadium carbides in (a) hydrogen concentration, (b) apparent diffusion coefficient, (c) permeation coefficient and (d) peak temperature during thermal desorption spectroscopy.

9 Conclusions

The following conclusions are outlined

- A unified modelling suite for hydrogen transport was introduced to describe electro-

chemical permeation, degassing and thermal desorption spectroscopy. The models, based on Fickian diffusion, showed to be valid in different steel grades including ferritic, martensitic, pearlitic, austenitic, as well as in polycrystalline nickel. This shows that the methodology can be employed as a tool for alloy and process design.

- The models presented in this work were shown to be equivalent to classical models for hydrogen diffusion and thermal desorption spectroscopy.

- The number density of trapping sites was found to be proportional to the mean spacing of the traps. This relationship was shown to hold for dislocations, grain boundaries and nano–scaled precipitates.

- The linear nature of Fickian diffusion allowed us to conclude that hydrogen kinetics under the presence of multiple kinds of traps can be described by adding the individual contribution of each trap for a moderate trap number density. However, the models for thermal desorption failed to fully predict the diffusion profiles in materials with a high number density of traps due to Fickian diffusion not accounting for interaction between traps. Extensions accounting for this limitation will be explored in future work.

- The apparent diffusion coefficient during permeation was shown to increase with increasing trapping capacity and charging current density; the latter increases the rate of electric charge passing through the sample and increasing the net mass flux.

- Systematic studies of different microstructural features affecting hydrogen diffusion in martensitic steels demonstrated that dislocations control the mobility of hydrogen, being these responsible to the increased susceptibility to hydrogen embrittlement of these steels.

Acknowledgements

Appendix

For a plate–shape specimen of width h, thickness w and length L we define the x and y axis as the directions of the specimen's width and thickness, respectively (Figure 2(b)) and the origin is located at the centre of the specimen. The boundary conditions for this configuration are: $c_{perm}(-h/2, y, z, t) = c_{perm}(h/2, y, z, t) = c_{perm}(x, -w/2, z, t) = c_{perm}(x, w/2, z, t) = c_{sat}$, $c_{perm}(x, y, -L/2, t) = c_{perm}(x, y, L/2, t) = c_{sat}$, $\frac{\partial c_{perm}}{\partial x}(-h/2, y, z, t) = \frac{\partial c_{perm}}{\partial x}(h/2, y, z, t) = \frac{\partial c_{perm}}{\partial y}(x, -w/2, z, t) = \frac{\partial c_{perm}}{\partial y}(x, w/2, z, t) = 0$, and $\frac{\partial c_{degas}}{\partial z}(x, y, -L/2, t) = \frac{\partial c_{degas}}{\partial z}(x, y, L/2, t) = 0$. The equation for permeation can be solved by separation of variables: $c_{perm} = \Theta_{klm} X_k(x) Y_l(y) Z_m(z)$, where X_k Y_l and Z_m depend only on x, y and z, respectively. A similar process can be followed for the case of degassing. The solutions of the mass transport during permeation, degassing and desorption are:

$$
\begin{aligned}
c_{perm}(x, y, z, t) &= c_{sat} \sum_{k,l,m=0}^{\infty} \left(1 - \exp(-D_{perm}(\beta_k^2 + \gamma_l^2 + \alpha_m^2)t)\right) X_k Y_l Z_m \\
c_{degas}(x, y, z, t) &= c_{0,degas} \sum_{k,l,m=0}^{\infty} \exp(-D(\beta_k^2 + \gamma_l^2 + \alpha_m^2)t) X_k Y_l Z_m \\
\frac{dc_{desorp}}{dt} &= c_{0,perm}\left(D + \frac{dD}{dt}t\right) \sum_{k,l,m=0}^{\infty} (\beta_k^2 + \gamma_l^2 + \alpha_m^2) \exp(-D(\beta_k^2 + \gamma_l^2 + \alpha_m^2)t) X_k Y_l Z_m
\end{aligned}
$$

$$(22)$$

with $\beta_k = \frac{\pi}{h}k$, $\gamma_l = \frac{\pi}{w}l$, and $X_k = \frac{4}{h\beta_k}\sin(\frac{\pi}{2}k)\cos(\beta_k x)$ and $Y_l = \frac{4}{w\gamma_l}\sin(\frac{\pi}{2}l)\cos(\gamma_l y)$ the eigenfunctions of the diffusion profiles.

References

[1] WY Choo and J Young Lee. Thermal analysis of trapped hydrogen in pure iron. *Metall Trans A*, 13:135–140, 1982.

[2] RA Oriani. The diffusion and trapping of hydrogen in steel. *Acta Metall*, 18:147–157, 1970.

38

[3] J Toribio and V Kharin. A generalised model of hydrogen diffusion in metal with multiple trap types. *Phil Mag*, 95:3429–3451, 2015.

[4] DL Johnson and JK Wu. Hydrogen transport in carbon steels as a function of carbon content and heat treatment near 298 k. *J Mater Energy Sys*, 8:402–408, 1987.

[5] JK Wu. Electrochemical method for studying hydrogen in iron, nickel and palladium. *Int J Hydrogen Energy*, 17:917–921, 1992.

[6] AB Hadžipašić, J Malina, and M Malina. The influence of microstructure on hydrogen diffusion and embrittlement of multiphase fine-grained steels with increased plasticity and strength. *Chem Biochem Eng Q*, 25:159–169, 2011.

[7] S Frappart, X Feaugas, J Creus, F Thebault, L Delattre, and H Marchebois. Hydrogen solubility, diffusivity and trapping in a tempered Fe-C-Cr martensitic steel under various mechanical stress states. *Mater Sci Eng A*, 534:384–393, 2012.

[8] WY Choo. Effect of cathodic charging current density on the apparent hydrogen diffusivity through pure iron. *J Mater Sci*, 19:2633–2638, 1984.

[9] SM Lee and JY Lee. The trapping and transport phenomena of hydrogen in nickel. *Metall Trans A*, 17:181–187, 1986.

[10] FD Fischer, J Svoboda, and E Kozeschnik. Interstitial diffusion in systems with multiple sorts of traps. *Model Sim Mater Sci Eng*, 21:025008, 2013.

[11] HE Kissinger. Reaction kinetics in differential thermal analysis. *Anal Chem*, 29:1702–1706, 1957.

[12] A McNabb and PK Foster. A new analysis of the diffusion of hydrogen in iron and ferritic steels. *Trans AIME*, 227:618–627, 1963.

[13] JB Leblond and D Dubois. A general mathematical description of hydrogen diffusion in steels–I. derivation of diffusion equations from boltzmann-type transport equations. *Acta Metall*, 31:1459–1469, 1983.

[14] JB Leblond and D Dubois. A general mathematical description of hydrogen diffusion in steels–II. numerical study of permeation and termination of trapping parameters. *Acta Metall*, 31:1471–1478, 1983.

[15] M Dadfarnia, P Sofronis, and T Neeraj. Hydrogen interaction with multiple traps: can it be used to mitigate embrittlement? *Int J Hydrogen Energy*, 36:10141–10148, 2011.

[16] EJ Song, DW Suh, and HKDH Bhadeshia. Theory for hydrogen desorption in ferritic steel. *Comp Mater Sci*, 79:36–44, 2013.

[17] JS Kim, YH Lee, DL Lee, KT Park, and CS Lee. Microstructural influences on hydrogen delayed fracture of high strength steels. *Mater Sci Eng A*, 505:105–110, 2009.

[18] T Doshida and K Takai. Dependence of hydrogen-induced lattice defects and hydrogen embrittlement of cold-drawn paralytic steels on hydrogen trap state, temperature, strain rate and hydrogen content. *Acta Mater*, 79:93–107, 2014.

[19] T Depover, O Monbaliu, E Wallet, and K Verbeken. Effect of Ti, Mo and Cr based precipitates on the hydrogen trapping and embrittlement of Fe-C-X Q&T alloys. *Int J Hydrogen Energy*, page In press, 2014.

[20] AJ Kumnick and HH Johnson. Deep trapping states for hydrogen in deformed iron. *Acta Metall*, 28:33–39, 1980.

[21] A Turnbull, RB Hutchings, and DH Ferriss. Modelling of thermal desorption of hydrogen from metals. *Mater Sci Eng A*, 238:317–328, 1997.

[22] S Frappart, X Feaugas, J Creus, F Thebault, L Delattre, and H Marchebois. Study of the hydrogen diffusion and segregation into Fe-C-Mo martensitic HSLA steel using electrochemical permeation test. *J Phys Chem Sol*, 71:1467?1479, 2010.

[23] BA Szost, RH Venter, and PEJ Rivera-Díaz-del-Castillo. Developing bearing steels combining hydrogen resistance and improved hardness. *Mater Des*, 43:499–506, 2013.

40

[24] W Solano-Alvarez, EJ Song, DK Han, DW Suh, and HKDH Bhadeshia. A generalised model of hydrogen diffusion in metal with multiple trap types. *Metall Mater Trans A*, 46:665–673, 2014.

[25] SS Chatterjee, BG Ateya, and HW Pickering. Effect of electrode posited metals on the permeation of hydrogen through iron membranes. *Metall Trans A*, 9:389–395, 1978.

[26] MH And Elhamid, BG Ateya, and HW Pickering. Determination of the rate constants of hydrogen absorption into metals. *J Electrochem Soc*, 147:2959–2963, 2000.

[27] S Wang, N Hashimoto, Y Wang, and S Ohnuki. Activation volume and density of mobile dislocations in hydrogen-charged iron. *Acta Mater*, 61:4734–4742, 2013.

[28] E Legrand, J Bouhattate, X Feaugas, and H Garmestani. Computational analysis of geometrical factors affecting experimental data extracted from hydrogen permeation tests: II - consequences of trapping and an oxide layer. *Int J Hydrogen Energy*, 37:13574–13582, 2012.

[29] E Legrand, A Oudriss, S Frappart, J Creus, X Feagas, and J Bouhattate. Computational analysis of geometrical factors affecting experimental data extracted from hydrogen permeation tests: III – Comparison with experimental results from the literature. *Int J Hydrogen Energy*, 39:1145–115, 2014.

[30] SM Charca, ONC Uwakweh, and VS Agarwala. Hydrogen transport conditions and effects in cathodic polarized AF1410 steel. *Metall Mater Trans A*, 38:2389–2399, 2007.

[31] K Kawakami and T Matsumiya. Numerical analysis of hydrogen trap state by TiC and V_4C_3 in bcc Fe. *ISIJ Int*, 52:1693–1697, 2012.

[32] DA Porter, KE Easterling, and M Sherif. *Phase transformations in metals and alloys*. CRC press, 2009.

[33] Y Furuya, E Hashimoto, and T Kino. Hydrogen permeation through nickel. *J J Appl Phys*, 23:1190–1196, 1984.

[34] A Oudriss, J Creus, J Bouhattate, E Conforto, C Berziou, V Savall, and X Feaugas. Grain size and grain-boundary effects on diffusion and trapping of hydrogen in pure nickel. *Acta Mater*, 60:6814–6828, 2012.

[35] MH And Elhamid, BG Ateya, and HW Pickering. Determination of the rate constants of hydrogen absortion into metals. *J Electrochem Soc*, 147:2959–2963, 2000.

[36] J Bouhattate, E Legrand, and X Feaugas. Computational analysis of geometrical factors affecting experimental data extracted from hydrogen permeation tests: I - consequences of trapping. *Int J Hydrogen Energy*, 36:12644–12652, 2011.

[37] WA Strauss. *Partial differential equations: an introduction*. John Wiley & Sons, 2008.

[38] J Xu, K Sun, WX Chen, and YY Li. Hydrogen permeation and diffusion in iron-base superalloys. *Acta Metall Mater*, 41:1455–1459, 1993.

[39] FG Wei and K Tsuzaki. Hydrogen absorption of incoherent TiC particles in iron from environment at high temperatures. *Metall Mater Trans A*, 35:3155–3163, 2004.

[40] FG Wei and K Tsuzaki. Quantitative analysis on hydrogen trapping of TiC particles in steels. *Metall Mater Trans A*, 37:331–353, 2006.

[41] D Pérez Escobar, E Wallet, L Duprez, A Atrens, and K Verbeken. Thermal desorption spectroscopy study of the interaction of hydrogen with TiC precipitates. *Met Mater Int*, 19:741–748, 2013.

[42] S Yamasaki and HKDH Bhadeshia. M_4C_3 precipitation in Fe-C-Mo-V steels and relationship to hydrogen trapping. *Proc R Soc A*, 462:2315–2330, 2006.

[43] K Kawakami and T Matsumiya. Ab-initio investigation of hydrogen trap state by cementite in bcc-Fe. *ISIJ Int*, 53:709–713, 2013.

42

[44] CJ Carneiro Filho, MB Mansur, PJ Modenesi, and BM Gonzalez. The effect of hydrogen release at room temperature on the ductility of steel wire rods for prestressed concrete. *Mater Sci Eng A*, 527:4947–4952, 2010.

[45] Y Liu, M Wang, and G Liu. Effect of hydrogen on ductility of high strength 3Ni-Cr-Mo-V steels. *Mater Sci Eng A*, 594:40–47, 2014.

[46] L Tau and SLI Chan. Effects of ferrite/pearlite alignment on the hydrogen permeation in a AISI 4130 steel. *Mater Letters*, 29:143–147, 1996.

[47] JK Tien, AW Thompson, IM Bernstein, and RJ Richards. Hydrogen transport by dislocations. *Metall Trans A*, 7:821–829, 1976.

[48] N Parvathavarthini, S Saroja, RK Dayal, and HS Khatak. Studies on hydrogen permeability of 2.25% Cr-1% Mo ferritic steel: correlation with microstructure. *J Nuc Mater*, 288:187–196, 2001.

[49] S Hinotani, Y Ohmori, and F Teriyaki. Effects of Fe_3C and Mo_2C precipitation on hydrogen diffusivity and hydrogen embrittlement in iron alloys. *Mater Sci Eng*, 76:57–69, 1985.

[50] EI Galindo-Nava and PEJ Rivera-Díaz-del-Castillo. Grain size evolution during discontinuous dynamic recrystallization. *Scripta Mater*, 72:1–4, 2014.

[51] M Nagumo, K Takai, and N Okuda. Nature of hydrogen trapping sites in steels induced by plastic deformation. *J Alloy Comp*, 293:310–316, 1999.

[52] DK Han, SK Lee, SJ Noh, SK Kim, and DW Suh. Effect of aluminium on hydrogen permeation of high-manganese twinning-induced plasticity steel. *Scripta Mater*, 99:45–48, 2015.

[53] O Yagodzinskyy, Y ad Todoshchenko, S Papula, and Hänninen. Hydrogen solubility and diffusion in austenitic stainless steels studied with thermal desorption spectroscopy. *Int J Hydrogen Energy*, 37:13574–13582, 2012.

[54] TP Perng and CJ Altstetter. Effects of deformation on hydrogen permeation in austenitic stainless steels. *Acta Metall*, 34:1771–1781, 1986.

[55] W Song, P Choi, G Inden, U Prahl, D Raabe, and W Bleck. On the spheroidized carbide dissolution and elemental partitioning in a high carbon bearing steel 100Cr6. *Metall Mater Trans A*, 45:595–606, 2014.

[56] ATW Barrow and PEJ Rivera-Díaz-del-Castillo. Nanoprecipitation in bearing steels. *Acta Mater*, 59:7155–7167, 2011.

[57] S Takaki. Limit of dislocation density and ultra-grain-refining on severe deformation in iron. *Int J ISSI*, 2:21–25, 2005.

[58] EI Galindo-Nava and PEJ Rivera-Díaz-del-Castillo. A model for the microstructure behaviour and strength evolution in lath martensite. *Acta Mater*, 98:81–83, 2015.

[59] EI Galindo-Nava and PEJ Rivera-Díaz-del-Castillo. Understanding the factors controlling the hardness in martensitic steels. *Scripta Mater*, 110:96–100, 2016.

[60] CH Young and HKDH Bhadeshia. Strength of mixtures of baiting and martensite. *Mater Sci Tech*, 10:209–214, 1994.

[61] N Guo, T Tiu, B Luan, B Wang, and Q Liu. Dislocation density and configuration in fully pearlitic steel during wire drawing. *Mater Res Innov*, 18:249–254, 2014.

[62] Y Hagi, H Hayashi and N Ohtani. Diffusion coefficient of hydrogen in pure iron between 230 and 300 K. *Trans JIM*, 20:349–357, 1979.

[63] HKDH Bhadeshia. Prevention of hydrogen embrittlement in steels. *ISIJ Int*, In press, 2015.

[64] M Dadfarnia, ML Martin, A Nagao, P Sofronis, and IM Robertson. Modeling of hydrogen transport by dislocations. *J Mech Phys Sol*, 78:511–525, 2015.

Effect of microstructure on H trapping and apparent diffusion coefficient